Check for updates

Dual ionic conductivity in Ba₃InGa₂O₇.₅: correlating structure and electrochemical properties

$Ba_3InGa_2O_{7.5}$

Oliver J. Wagstaff, ⓘ * Archie D. Collins, John S. O. Evans and
Ivana Radosavljević Evans ⓘ

Perovskite-related materials derived from the brownmillerite-type $Ba_2In_2O_5$ and those with the formula $A_3OhTd_2O_{7.5}$ (A = 2^+ cation, Oh = octahedral 3^+ cation, Td = tetrahedral 3^+ cation) are two distinct classes of ionic conductors. We report the synthesis of $Ba_3InGa_2O_{7.5}$, a material spanning these families that demonstrates promising electrochemical behaviour. X-ray powder diffraction analysis shows it adopts a monoclinic $P2/c$ structure at room temperature (a = 7.9557(13) Å, b = 5.8762(9) Å, c = 18.2237(3) Å and β = 91.570(1)°) and undergoes a phase transition to space group $Cmcm$ at 600 °C. Humidified variable temperature X-ray powder diffraction and thermogravimetric analysis demonstrate that $Ba_3InGa_2O_{7.5}$ can uptake significant amounts of H_2O without decomposition when exposed to moisture-rich atmospheres. Complex impedance studies reveal dual ionic conductivity, with either proton or oxide ion transport dominating depending on temperature and experimental conditions. $Ba_3InGa_2O_{7.5}$ exhibits the highest total conductivity for an unsubstituted $A_3OhTd_2O_{7.5}$-type material.

Introduction

Materials displaying ionic conductivity through proton or oxide ion mobility are important in several developing technologies such as separation membranes, fuel reformers, sensors, super-capacitors and as electrolyte materials for solid oxide fuel cells (SOFCs).[1–6] Adoption of SOFCs at large-scale is hindered by the high temperatures (> 700 °C) at which conventional electrolyte materials, such as yttria-stabilised zirconia and gadolinia-doped ceria, exhibit sufficient ionic conductivity for use in fabricated devices.[7,8] The identification of materials that conduct at intermediate or low temperatures is important for the wider application of these technologies.

Various perovskite and perovskite-related materials have been investigated for exhibiting oxide ion, proton, mixed ionic and even triple ($O^{2-}/e^-/H^+$) conductivity at different temperatures.[9–12] Examples include the proton conducting barium zirconates and cerates (~300–600 °C) or W^{6+}-doped $BaScO_{2.5}$ (< 400 °C), oxide ion conducting $La_{0.8}Sr_{0.2}Ga_{0.8}Mg_{0.2}O_{3-\delta}$ (~500–900 °C) and $Ba_3MoNbO_{8.5}$ (500–600 °C), and dual conducting $Ba_7Nb_4MoO_{20}$ (300–800 °C).[13–20]

Brownmillerite-type materials are a perovskite-related structural family that have been studied as both ionic and mixed ionic-electronic conductors depending on composition.[21–24] The brownmillerite structure is derived from the cubic perovskite through the replacement of one-sixth of the oxide ions with vacancies.

Department of Chemistry, Durham University, Lower Mountjoy, Durham DH1 3LE, UK. E-mail: ivana.radosavljevic@durham.ac.uk

The ordered vacancies produce alternating layers of BO_4 and BO_6 polyhedra, with individual BO_4 tetrahedra connecting to form chains along one direction of the unit cell. At higher temperatures it is possible for these vacancies to disorder to produce first tetragonal and then cubic structures.[25] A marked increase in oxide ion conductivity often accompanies the disorder, illustrated by $Ba_2In_2O_5$.[26] The conductivity of $Ba_2In_2O_5$ sharply increases from a modest $\sigma \sim 10^{-3}$ S cm^{-1} at 800 °C to 0.1 S cm^{-1} at ~940 °C through this transition. Attempts to stabilise the disordered phases to room temperature *via* partial substitution of In^{3+} (*e.g.* Ln^{3+}, Zr^{4+}, Ti^{4+}, Mo^{5+}) have been successful, but are often associated with decreases in maximum conductivity.[27–30]

Separately, it has been found that $Ba_2In_2O_5$ converts to a series of hydrated $Ba_2In_2O_5(H_2O)_y$ ($0 < y < 1$) orthorhombic phases when annealed in wet atmospheres. These phases exhibit dual protonic-oxide ion below 400 °C.[31–36]

Investigations of the solid solution $Ba_2(In_{1-x}Ga_x)_2O_5$ have demonstrated the lowering of the order–disorder transition to <800 °C ($x \leq 0.2$), and stabilisation of a disordered cubic phase to room temperature ($0.25 \leq x \leq 0.45$).[37–39] The material with an equal amount of In and Ga ($x = 0.5$) has been found to adopt both the cubic disordered phase and an ordered brown-millerite phase (with octahedral In^{3+} and tetrahedral Ga^{3+}) depending on the annealing temperature.[40] The maximum total conductivity of these materials decreases with Ga^{3+} content, although all except Ba_2InGaO_5 exhibit higher conductivity than $Ba_2In_2O_5$ in the intermediate temperature range (500–800 °C). The conductivity of Ba_2InGaO_5 is almost two orders of magnitude lower than $Ba_2In_2O_5$ at 800 °C, a result of the reduced oxygen

vacancy mobility induced by the cation ordering.[40,41] Additionally, Ba_2InGaO_5 displays a small amount of proton conductivity ($\sigma \sim 10^{-7}$ S cm^{-1}) below 500 °C.

Only limited work beyond the midpoint of the $In_{1-x}Ga_x$ solid solution range exists, with the hypothetical end member $Ba_2Ga_2O_5$ reported as thermodynamically unstable with respect to a mixture of BaO and $BaGa_2O_4$.[42,43] Increasing the Ga-content to $x = 2/3$ would produce a compound isoformulaic with a structurally-distinct class of perovskite derived ionic conductors: the $A_3OhTd_2O_{7.5}$ materials (A = 2^+ cation, Oh = octahedral 3^+ cation, Td = tetrahedral 3^+ cation).

Similarly to the brownmillerites, $A_3OhTd_2O_{7.5}$ compounds display varied transport properties dependent on composition, with the donor-doped $Ba_{2.9}La_{0.1}YGa_2O_{7.55}$ exhibiting pure oxide ion conductivity whilst the acceptor-doped $Ba_{1.5}Sr_{1.5}YGa_{1.8}Zn_{0.2}O_{7.4}$ and $Sr_3YGa_{1.8}Zn_{0.2}O_{7.4}$ display majority proton conductivity in the intermediate temperature region ($\leq$ 800 °C).[44–47] Given the superior electrochemical performance of $Ba_2In_2O_5$-based conductors, it is of interest to expand the $Ba_2(In_{1-x}Ga_x)_2O_5$ series to $x = 2/3$ and investigate the properties of $Ba_3InGa_2O_{7.5}$. One previous study on this material suggests that it may be a moderate dual ionic conductor ($\sigma \sim 10^{-4}$ S cm^{-1} at 800 °C).[48] However, the measurements reported were carried out on a sample that contained unidentified impurities, warranting further investigation.

In the present work we explore the new $A_3OhTd_2O_{7.5}$ ionic conductor $Ba_3InGa_2O_{7.5}$ to investigate its electrochemical properties, and report a sample with maximum total conductivity amongst the largest for $A_3OhTd_2O_{7.5}$ materials that also exhibits dual oxide ion and proton conductivity. The average structure between room temperature and 1000 °C is studied using X-ray powder diffraction. The conductivity is investigated using electrochemical impedance spectroscopy, and additional information on moisture uptake is gained through thermogravimetric analysis.

Experimental

Sample preparation

Polycrystalline samples of $Ba_3InGa_2O_{7.5}$ ($\sim$ 2 g) were initially prepared from stoichiometric amounts of $BaCO_3$ (Sigma-Aldrich, $\geq$99.9%), In_2O_3 (Sigma-Aldrich, 99.99%) and Ga_2O_3 (Sigma-Aldrich, $\geq$99.99%) based on the method of Kochetova et al.[48] Reagents were mixed and ground together under ethanol, then heated in alumina crucibles for up to 108 h at 1200 °C with a heating and cooling rate of 5 °C min^{-1}. Intermediate regrinding and pelleting were carried out until powder X-ray diffraction patterns of each sample were constant. An off-white powder was obtained. Subsequent syntheses aimed at increasing product purity were modified by adjusting the relative amounts of starting reagents so that 95 wt% of stoichiometric Ga_2O_3 was used (giving a Ba : In : Ga molar ratio in the starting reagents of 3 : 1 : 1.91).

Structural characterisation

Ambient X-ray diffraction data were collected on a Bruker D8 advance powder diffractometer in Bragg–Brentano geometry using Cu Kα radiation and a Lynx-eye detector. Measurements for final Rietveld analysis were collected with a 2θ range of $10° \leq 2\theta \leq 120°$.

Variable temperature X-ray diffraction patterns were recorded with an Anton Parr HTK1200 furnace attachment. X-ray diffraction patterns were collected on heating and cooling at 20 °C intervals between 25 and 1000 °C over a 2θ range of $10 \leq 2\theta \leq 90°$. Collection times were 30 minutes at each temperature. A final pattern was collected for 12h at 1000 °C. A further series of measurements were collected under flowing wet nitrogen ($pH_2O \sim 0.02$ atm) between 25 and 1000 °C with two heating regimes: 20 °C intervals on heating and cooling for 25–500 °C, and 160 °C intervals for 500–1000 °C. Furnace temperatures were calibrated using an external alumina standard. Analysis was carried out via Rietveld refinement implemented in the TOPAS Academic software.[49–51]

Electrochemical characterisation

For impedance spectroscopy a sample of $Ba_3InGa_2O_{7.5}$ was pressed into a 10 mm pellet and sintered to achieve a high density (a pressure of 5 tonnes and sintering at 1200 °C for 50 h achieved a relative density of 85%). Platinum ink (Metalor) was applied to the face of the pellet before mounting on a Probostat A-6 cell placed inside a vertically oriented tube furnace. Platinum wire electrodes were attached to each face and set by heating to 1000 °C for 30 min. Impedance measurements were collected at $\sim$20 °C intervals on heating and cooling between 20 and 1000 °C at 2 °C min^{-1} using a Solartron 1260 frequency response analyser in the range of 10^{-1}–10^7 Hz. Further measurements were carried out under both dry and wet flowing nitrogen ($pH_2O \sim 0.02$ atm) with multiple cycles of heating and cooling to ensure equilibrium had been achieved. The results were analysed using the ZView/ZPlot Software (Scribner Associates).

Thermogravimetric analysis

Mass changes were measured using a PerkinElmer Thermogravimetric Analysis (TGA) 8000 instrument. A powdered sample of $Ba_3InGa_2O_{7.5}$ was heated and cooled between 30 and 1000 °C at a rate of 10 °C min^{-1} under flowing air.

Results and discussion

Synthesis

Powder diffraction patterns of samples of $Ba_3InGa_2O_{7.5}$ produced using stoichiometric reagent amounts at 1200 °C were similar to those previously reported.[48] Fitting the data with the $P2/c$ structural model of $Ba_3ErGa_2O_{7.5}$[52] (Fig. 1) accounted for the majority of the observed peaks. However, two observed weak peaks at $2\theta \sim 28.0$ and 33.2° were not predicted by this model (Fig. S1). Instead, these peaks were readily fitted by including $BaGa_2O_4$ as a secondary phase that made up $\sim$10 wt% of the sample. Further heating of this sample for a total period in excess of 100 h did not decrease the $BaGa_2O_4$ weight percentage, whilst raising the synthesis temperature to 1300 °C resulted in melting. Our results suggest that the sample of $Ba_3InGa_2O_{7.5}$ previously reported was

≤90% pure instead of the single phase claimed. By contrast, our modified synthesis procedure, using 95 wt% of stoichiometric Ga_2O_3 resulted in a sample with >98 wt% $Ba_3InGa_2O_{7.5}$ after heating at 1200 °C for 108 h. This suggests that some Ba- and In-volatilisation occurs at the high reaction temperature.

Room temperature structure

The powder X-ray diffraction pattern of $Ba_3InGa_2O_{7.5}$ was fitted with the $P2/c$ structural model of $Ba_3ErGa_2O_{7.5}$. This is a 12-fold superstructure of the cubic perovskite ($2a_p \times \sqrt{2}a_p \times 3\sqrt{2}a_p$) with the octahedra (Oh) and tetrahedra (Td) ordered to give layers of corner-sharing Ga_2O_7 tetrahedra separated by slabs of $[(GaO_4)(InO_6)]_2$ (Fig. 1). All peaks were fitted satisfactorily with this model except two low-intensity peaks at 28.0 and 33.2°, which were accounted for by the inclusion of 1.7(2) wt% $BaGa_2O_4$.

Refinement of the fractional occupancies of the Oh and Td sites confirmed the expected overall In:Ga ratio of 1:2 but indicated that partial In/Ga disorder occurs between the Oh and Td_2O_7 sites with the Td site in the slab occupied entirely by Ga^{3+}. This is consistent with the bonding preferences of these species, with In^{3+} and Ga^{3+} known to adopt both tetrahedral and octahedral geometries.[53,54] The use of a model where the total occupancies of In^{3+} and Ga^{3+} across the sites was constrained to unity showed no difference compared to one with freely refined occupancies. Final refined occupancies gave an In:Ga ratio of 0.86(2):0.14(2) for the Oh site and the reverse for the Td site. Inclusion of the partial disorder resulted in a weighted R-factor (R_{wp}) of 2.130%, compared with 2.152% for the fully ordered structural model. A single isotropic atomic displacement parameter was used for each atom type, except for the partially occupied sites which used an equated value. Some small anisotropic strain broadening was accounted for using the peak shape model described by Stephens.[55] Cell parameters of $a = 7.9557(13)$ Å, $b = 5.8762(9)$ Å, $c = 18.2237(3)$ Å and $\beta = 91.570(1)°$ were obtained with the final fit shown in Fig. 2a. Crystallographic parameters for $Ba_3InGa_2O_{7.5}$ are given in Table S1.
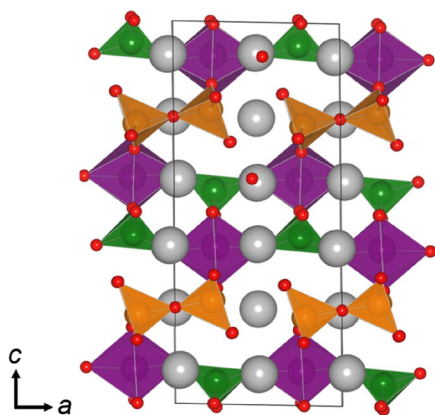
High temperature structure

Materials in the $A_3OhTd_2O_{7.5}$ family are known to undergo phase transitions as a function of temperature.[45–47,52,56] Unit-cell parameters of $Ba_3InGa_2O_{7.5}$ between room temperature and 1000 °C were therefore determined from variable temperature X-ray powder diffraction patterns analysed by Rietveld fitting (Fig. 3a). Three distinct regions of cell parameter behaviour can be identified. Between 25 and 400 °C the b- and c-cell axes increase linearly whilst the a-axis initially expands before contracting between 320 and 400 °C (Fig. 3b). Similarly to the a-axis, the monoclinic angle (β) remains approximately constant below 320 °C then begins to decrease. This is likely related to moisture uptake/loss by $Ba_3InGa_2O_{7.5}$, as is the case for some other $A_3OhTd_2O_{7.5}$ materials.[45,46] This process must be rapid and on the timescale of the measurements (~30 min), as the behaviour is reversible on both heating and cooling. Between 400 and ~570 °C the three unit-cell axes and the monoclinic angle evolve linearly. From 570 °C the monoclinic angle rapidly decreases to 90° coinciding with subtle discontinuities in the a-, b-, and c-axes, suggesting a monoclinic-to-orthorhombic phase transition. The extracted volumetric thermal expansion coefficient (Fig. 3c) is consistent with this interpretation. There is a small feature around 200–400 °C, caused by moisture uptake and loss as
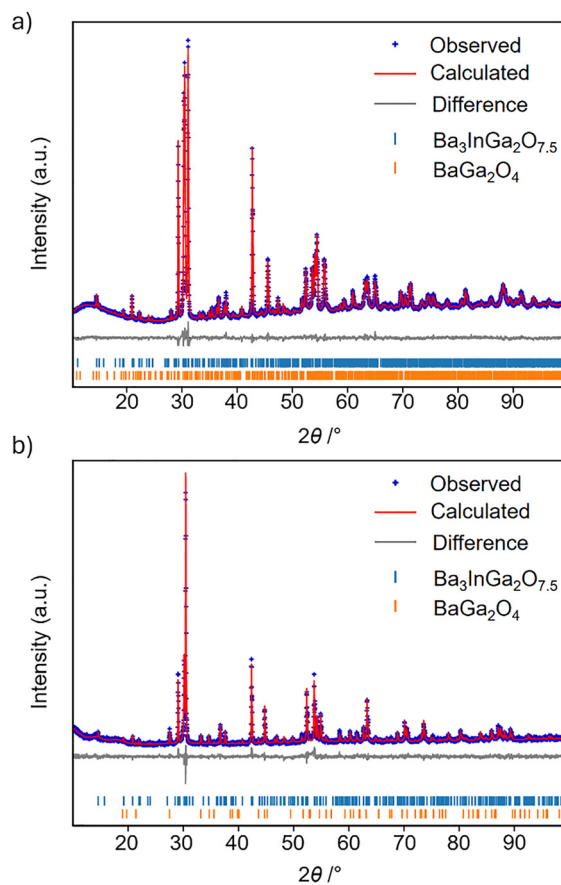

Fig. 1 View of the $P2/c$ structure of $A_3OhTd_2O_{7.5}$ materials (A^{2+} in grey, Oh^{3+} in purple, Td^{3+} in green/orange and O^{2-} in red).
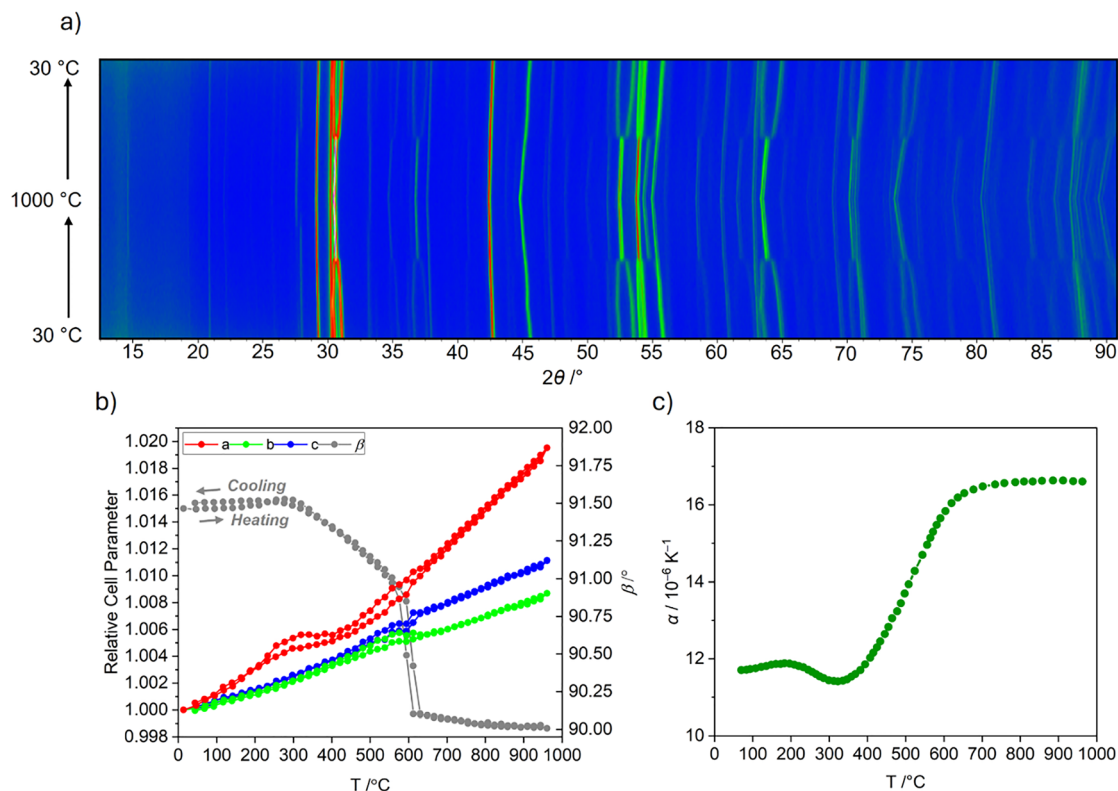

Fig. 2 Rietveld refinements against laboratory powder X-ray diffraction pattern of $Ba_3InGa_2O_{7.5}$ (a) At room temperature in space group $P2/c$. (b) At 1000 °C in space group $Cmcm$.

Fig. 3 (a) Powder X-ray diffraction patterns of $Ba_3InGa_2O_{7.5}$, viewed as a colour map where blue and red correspond to regions of low and high intensity, as a function of temperature between 30 and 1000 °C. (b) Relative unit-cell axes and absolute monoclinic angle as a function of temperature during heating and cooling. (c) Volumetric thermal expansion coefficient, plotted as $^{1/3}\alpha_V$. Errors plotted in both (b) and (c) are smaller than the size of individual points.

in other compounds.[45,46,57] The thermal expansion then increases approximately linearly until the phase transition at 600 °C.

Inspection of the diffraction patterns also confirms the presence of the 1.7(2) wt% secondary $BaGa_2O_4$ phase. A discontinuity occurs at around 800 °C for the peaks at $2\theta \sim 28$ and 33°, which is associated with the known phase transition from the $P6_3$ α-phase to the $P6_322$ β-phase (Fig. S2).[43,58]

Unlike for $Ba_3YGa_2O_{7.5}$, no thermal hysteresis is associated with the monoclinic-to-orthorhombic transition temperature of $Ba_3InGa_2O_{7.5}$.[47] However, the phase transition is characterised by the merging of several reflections including the most intense $(21\bar{3})$ and (213) peaks around $2\theta \sim 31°$. Therefore, one sensible starting model for the high-temperature structure of $Ba_3InGa_2O_{7.5}$ is the $P2_1/a$ model of $Ba_3YGa_2O_{7.5}$ that appears orthorhombic due to a monoclinic angle ($\gamma \sim 107.8°$) which transforms to almost exactly 90° in the $P2/c$ setting (Fig. S3a).[47,59] An alternative description is the orthorhombic $Cmcm$ model adopted by $Ba_{1.5}Sr_{1.5}YGa_2O_{7.5}$, in which disorder exists along the Td_2O_7 chains (Fig. S3b).[46] Rietveld refinements of both of these models against the highest temperature X-ray diffraction pattern show similar quality fits, with all major peaks accounted for by both models. The R_{wp} for the fit in $P2_1/a$ is marginally lower (6.63 *vs.* 6.90%); however, several weak peaks that are present above the phase transition for $Ba_3YGa_2O_{7.5}$ are not evident in the $Ba_3InGa_2O_{7.5}$ patterns. (Fig. S4). These peaks are not predicted for the $Cmcm$ model. Accordingly, we assign the $Cmcm$ model to

the high-temperature structure of $Ba_3InGa_2O_{7.5}$, with cell parameters of $a = 5.9251(3)$ Å, $b = 18.4230(7)$ Å, $c = 8.0957(3)$ Å. Refinement of partial In/Ga occupancies showed a ratio of 0.88(3):0.12(3) at the octahedral interslab site, consistent with the value obtained at room temperature. The final fit, shown in Fig. 2b with crystallographic parameters in Table S2, gave an R_{wp} of 6.90%.

Moisture uptake

Proton conductivity in oxygen-deficient perovskite-type materials is often driven by moisture uptake, through deliberate exposure during fabrication or testing, or from the ambient environment whilst stored. Uptake during storage is especially important as it can lead to sample degradation limiting electrochemical performance.[60–62] Thermogravimetric analysis (TGA) shows that a sample of $Ba_3InGa_2O_{7.5}$ exposed to laboratory atmosphere for several days experiences a $\sim 0.4\%$ mass loss (equivalent to ~ 1.7 moles of H_2O per $Ba_3InGa_2O_{7.5}$ formula unit) by 375 °C on heating (Fig. S5), consistent with the behaviour observed in the variable temperature powder diffraction. The mass then remains approximately constant on heating to 1000 °C and cooling to room temperature. Despite the moisture uptake, $Ba_3InGa_2O_{7.5}$ remains stable for extended periods when stored in closed containers.

Both the TGA and conductivity exhibited under wet atmospheres (below) demonstrate that $Ba_3InGa_2O_{7.5}$ can take up moisture under suitable conditions. To investigate whether

$Ba_3InGa_2O_{7.5}$ forms a structurally distinct hydrated phase similar to $Ba_2In_2O_5$, variable temperature diffraction patterns were collected under wet flowing nitrogen. The patterns demonstrate that the $P2/c$ structure persists until the $Cmcm$ phase transition at 600 °C (Fig. S6). The extracted cell parameters are larger for each cell axis below 500 °C under humid conditions relative to those in air (Fig. S7), confirming the uptake of H_2O. The a-axis (parallel to the Td_2O_7 chains) increases by the largest amount, which agrees with previous observations of moisture uptake in $Sr_3YGa_{1.8}Zn_{0.2}O_{7.4}$ and $Ba_3YGa_{1.8}Zn_{0.2}O_{7.4}$.[46,47] This suggests that water molecules occupy vacant sites within the Td_2O_7 layers. These layers have been associated with long range ionic mobility in $A_3OhTd_2O_{7.5}$-type materials.[46]

Conductivity

The conductivity of $Ba_3InGa_2O_{7.5}$ was measured in air and under flowing dry and wet nitrogen from ~250 to 1000 °C. The complex plane plots at all temperatures showed two responses, an electrode response at low frequencies and a semicircular one at high frequencies (Fig. S8). The forms of these responses changed with temperature. At lower temperatures (<400 °C), overlapping responses formed a depressed semicircle followed by a 45° spike. At higher temperatures a single semicircular signal was observed, whilst the electrode response tapered into an arc. The evolution of the electrode response is typical for finite Warburg type diffusion and majority ionic conductivity.[63,64] The capacitance was extracted from the apex of the arc using the relationship $\omega RC = 1$. This gave a value of ~10^{-12} F cm^{-1}, indicating a bulk response.[63] The total conductivity at all temperatures was derived from the resistance given by the intercept with the real axis.[65]

Arrhenius plots of the total conductivities are shown in Fig. 4. In air the maximum total conductivity is 2.6×10^{-3} S cm^{-1}. This is an order of magnitude higher than other unsubstituted $A_3OhTd_2O_{7.5}$ materials and comparable to the maximum conductivity of the best ionic conductor in this material family, $Ba_{2.9}La_{0.1}YGa_2O_{7.55}$.[47] The behaviour is likely due to the presence

of In^{3+} within the Td_2O_7 chains, which stabilise migrating species through temporary coordination to the metal centre. The conductivity is greater than that reported by Kochetova *et al.* at comparable temperatures (> 500 °C).[48] This could be due to different sample relative density (not stated in that work) but is likely due to the ~10% $BaGa_2O_4$ present in the previous work.

The Arrhenius curve can be separated into three regions with distinct gradients: $T > 700$ °C, $350 < T < 700$ °C, and $T < 350$ °C. The boundaries of these regions approximately align with the $P2/c \leftrightarrow Cmcm$ phase transition and the loss of moisture as determined from TGA. There is no abrupt increase in conductivity at the $P2/c \leftrightarrow Cmcm$ phase transition temperature. This suggests that despite the O1 disorder in the $Cmcm$ structural model, individual Td_2O_7 chains remain locally ordered at high temperature, preserving the $-Td-O-Td-\square-$ arrangement. This is consistent with other $A_3OhTd_2O_{7.5}$-type conductors.[44,45,47,56] Local disorder within these chains would require that some $-\square-Td-\square-$ units are formed. Such 3-coordinate TdO_3 units were not observed in *ab initio* molecular dynamics simulations.[46]

Activation energies were determined from plots of $\ln(\sigma T)$ against $1/T$. Above 700 °C the activation energy was 0.97(2) eV, a value consistent with oxide ions being the majority charge carrier.[66–68] Between 400 and 700 °C a proton component due to moisture uptake is likely as the activation energy decreases to 0.58(1) eV. This is confirmed by measurements on a pre-dried sample in dry N_2 that showed similar conductivity to that in air above 700 °C (majority oxide ion conductivity), whilst below 700 °C the conductivity was substantially lower with minimal change in gradient.

Fig. 4b compares conductivity data collected in air with data collected under wet N_2. A bump was observed on heating under wet N_2 between ~330 and 470 °C, whilst on cooling there is a plateau over the same temperature range (Fig. 4b). The behaviour under wet conditions was reproducible through multiple heating and cooling cycles. The hysteresis of conductivity due to the gain and loss of protons is similar to that for other substituted barium indate systems.[29,69,70] On heating the
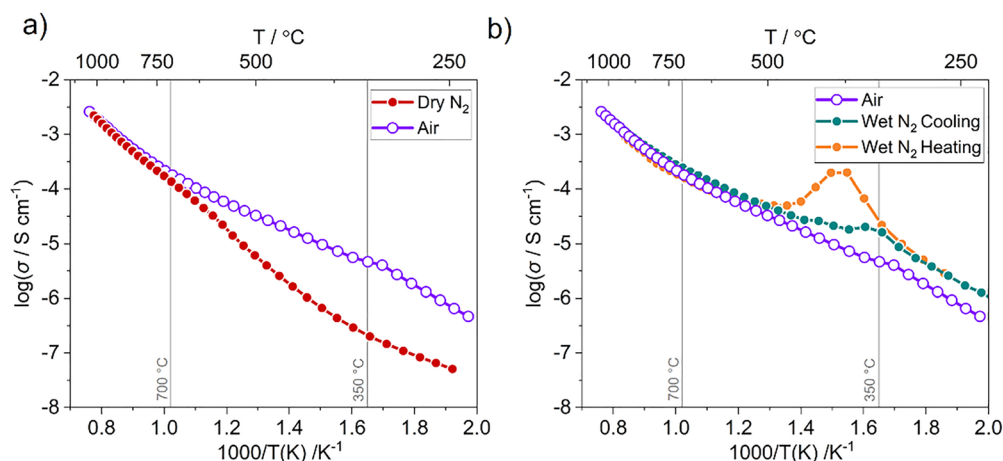

Fig. 4 (a) Conductivity in air (purple, empty) and dry N_2 (red, filled) (b) conductivity in wet N_2 on heating (orange, filled) and cooling (blue, filled) of $Ba_3InGa_2O_{7.5}$. Vertical grey lines at 350 and 700 °C separate the three conductivity regions with distinct gradients for the measurements collected under air.

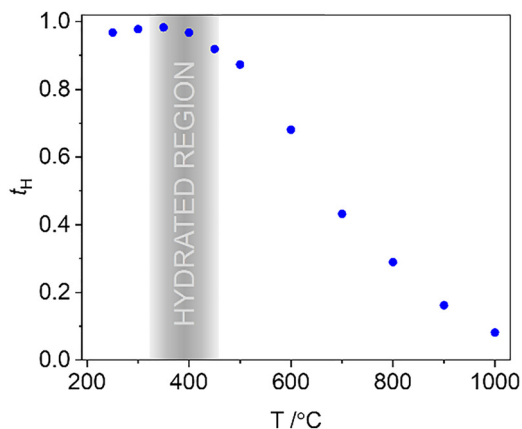**Fig. 5** Proton transport numbers calculated from the total conductivity in wet and dry N_2 of $Ba_3InGa_2O_{7.5}$.

increasing mobility of the protons with temperature is counteracted by their loss after 380 °C, resulting in a decrease in the total number of charge carriers. Beyond ~ 700 °C the conductivity under wet N_2 converges with the measurements collected under air and dry N_2. Approximate proton transport numbers were calculated from the data measured under wet and dry N_2 across the measured temperature range (Fig. 5) *via* $t_H = (\sigma_{wet} - \sigma_{dry})/\sigma_{wet}$. These confirm that protons dominate conductivity at lower temperatures and remain the majority charge carrier until 700 °C. By 1000 °C the conductivity is almost entirely oxide-derived in nature ($t_H < 0.09$). The low temperature moisture uptake is also presumably responsible for the slight bump in the conductivity measured in air at ~ 350 °C, due to small amounts of atmospheric moisture.

The conductivity of $Ba_3InGa_2O_{7.5}$ is lower than that for the $Ba_2(In_{1-x}Ga_x)_2O_5$ materials with $0.1 \leq x \leq 0.45$ between 500 and 1000 °C.[37–39,41] This is likely the result of the persistence of oxide vacancy ordering at high temperatures. However, the conductivity is comparable to $Ba_2In_2O_5$ in the brownmillerite temperature region (<800 °C) and significantly higher than that reported for Ba_2InGaO_5.[26,40]

Conclusions

$Ba_3InGa_2O_{7.5}$ was prepared by conventional solid-state synthesis. X-ray diffraction analysis indicates that it adopts the monoclinic $P2/c$ structure of other Ba-containing $A_3OhTd_2O_{7.5}$ materials at room temperature instead of the orthorhombic brownmillerite or cubic perovskite structures of other members of the $Ba_2(In_{1-x}Ga_x)_2O_5$ solid solution. Despite there being partial In/Ga disorder, refinements show that the In:Ga ratio is the targeted 1:2. Variable temperature powder diffraction studies show a reversible discontinuous monoclinic-to-orthorhombic phase transition at 600 °C and measurable moisture uptake below 400 °C; this was confirmed by thermogravimetric analysis. Despite the moisture uptake, $Ba_3InGa_2O_{7.5}$ remains stable when exposed to deliberately humidified atmospheres and can be stored without decomposition for periods of at least several weeks.

Impedance spectroscopy shows $Ba_3InGa_2O_{7.5}$ to be a dual ionic conductor, exhibiting both oxide ion and proton conductivity. The maximum total conductivity is the highest reported for an unsubstituted $A_3OhTd_2O_{7.5}$ conductor (2.6×10^{-3} S cm^{-1}). The atmospheric moisture content used for the experiments has a significant impact on the conductivity. Below 400 °C proton conductivity dominates under humidified conditions, reaching a maximum of 2×10^{-4} S cm^{-1}. Dual oxide ion and proton conductivity exists between 400 and ~ 750 °C, whilst oxide ion conductivity dominates at the highest temperatures, as well as under dry conditions.

Overall, the conductivity behaviour reflects a crossover from proton to oxide ion transport. This leads to $Ba_3InGa_2O_{7.5}$ having the highest total conductivity of any $A_3OhTd_2O_{7.5}$-type conductor at intermediate temperatures, in addition to remaining competitive at higher temperatures.

Conflicts of interest

There are no conflicts to declare.

Data availability

Additional data supporting this article are included in the supplementary information (SI). Supplementary information is available. See DOI: https://doi.org/10.1039/d5ma01495f.

Acknowledgements

References

1 N. N. M. Tahir, N. A. Baharuddin, A. A. Samat, N. Osman and M. R. Somalu, *J. Alloys Compd.*, 2022, **894**, 162458.

2 P. Colomban, *Solid State Ion.*, 2019, **334**, 125–144.

3 P. J. Megía, A. J. Vizcaíno, J. A. Calles and A. Carrero, *Energy Fuels*, 2021, **35**, 16403–16415.

4 L. Malavasi, C. A. J. Fisher and M. S. Islam, *Chem. Soc. Rev.*, 2010, **39**, 4370.

5 J. B. Goodenough, *Nature*, 2000, **404**, 821–823.

6 D. J. L. Brett, A. Atkinson, N. P. Brandon and S. J. Skinner, *Chem. Soc. Rev.*, 2008, **37**, 1568.

7 D. Pérez-Coll, E. Sánchez-López and G. C. Mather, *Solid State Ion.*, 2010, **181**, 1033–1042.

8 J. P. Goff, W. Hayes, S. Hull, M. T. Hutchings and K. N. Clausen, *Phys. Rev. B: Condens. Matter Mater. Phys.*, 1999, **59**, 14202–14219.

9 M. Papac, V. Stevanović, A. Zakutayev and R. O'Hayre, *Nat. Mater.*, 2021, **20**, 301–313.

10 Y. Zhang, R. Knibbe, J. Sunarso, Y. Zhong, W. Zhou, Z. Shao and Z. Zhu, *Adv. Mater.*, 2017, **29**, 1700132.

11 S. Fop, *J. Mater. Chem. A*, 2021, **9**, 18836–18856.

12 X. Yang, A. J. Fernández-Carrión and X. Kuang, *Chem. Rev.*, 2023, **123**, 9356–9396.

13 L. Yang, S. Wang, K. Blinn, M. Liu, Z. Liu, Z. Cheng and M. Liu, *Science*, 2009, **326**, 126–129.

14 K. Saito, K. Umeda, K. Fujii, K. Mori and M. Yashima, *J. Mater. Chem. A*, 2024, **12**(22), 13310–13319.

15 M. Morales, J. J. Roa, J. Tartaj and M. Segarra, *J. Eur. Ceram. Soc.*, 2016, **36**, 1–16.

16 S. Fop, J. M. S. Skakle, A. C. McLaughlin, P. A. Connor, J. T. S. Irvine, R. I. Smith and E. J. Wildman, *J. Am. Chem. Soc.*, 2016, **138**, 16764–16769.

17 J. E. Auckett, K. L. Milton and I. R. Evans, *Chem. Mater.*, 2019, **31**, 1715–1719.

18 S. Fop, K. S. McCombie, E. J. Wildman, J. M. S. Skakle, J. T. S. Irvine, P. A. Connor, C. Savaniu, C. Ritter and A. C. Mclaughlin, *Nat. Mater.*, 2020, **19**, 752–757.

19 M. Yashima, T. Tsujiguchi, Y. Sakuda, Y. Yasui, Y. Zhou, K. Fujii, S. Torii, T. Kamiyama and S. J. Skinner, *Nat. Commun.*, 2021, **12**, 556.

20 T. Ishihara, H. Matsuda and Y. Takita, *J. Am. Chem. Soc.*, 1994, **116**, 3801–3803.

21 F. Ramezanipour, J. E. Greedan, A. P. Grosvenor, J. F. Britten, L. M. D. Cranswick and V. O. Garlea, *Chem. Mater.*, 2010, **22**, 6008–6020.

22 P. Jiang, J. Li, A. Ozarowski, A. W. Sleight and M. A. Subramanian, *Inorg. Chem.*, 2013, **52**, 1349–1357.

23 C. A. Fuller, Q. Berrod, B. Frick, M. R. Johnson, S. J. Clark, J. S. O. Evans and I. R. Evans, *Chem. Mater.*, 2019, **31**, 7395–7404.

24 C. A. Fuller, Q. Berrod, B. Frick, M. R. Johnson, M. Avdeev, J. S. O. Evans and I. R. Evans, *Chem. Mater.*, 2020, **32**, 4347–4357.

25 S. A. Speakman, J. W. Richardson, B. J. Mitchell and S. T. Misture, *Solid State Ion.*, 2002, **149**, 247–259.

26 J. B. Goodenough, J. E. Ruiz-Diaz and Y. S. Zhen, *Solid State Ion.*, 1990, **44**, 21–31.

27 T. Q. Ta, T. Tsuji and Y. Yamamura, *J. Alloys Compd.*, 2006, **408–412**, 253–256.

28 P. Berastegui, S. Hull, F. J. García-García and S.-G. Eriksson, *J. Solid State Chem.*, 2002, **164**, 119–130.

29 V. Jayaraman, A. Magrez, M. Caldes, O. Joubert, M. Ganne, Y. Piffard and L. Brohan, *Solid State Ion.*, 2004, **170**, 17–24.

30 A. Rolle, R. N. Vannier, N. V. Giridharan and F. Abraham, *Solid State Ion.*, 2005, **176**, 2095–2103.

31 G. B. Zhang and D. M. Smyth, *Solid State Ion.*, 1995, **82**, 153–160.

32 T. Schober, J. Friedrich and F. Krug, *Solid State Ion.*, 1997, **99**, 9–13.

33 W. Fischer, G. Reck and T. Schober, *Solid State Ion.*, 1999, **116**, 211–215.

34 M. Karlsson, A. Matic, C. S. Knee, I. Ahmed, S. G. Eriksson and L. Börjesson, *Chem. Mater.*, 2008, **20**, 3480–3486.

35 A. Perrichon, M. M. Koza, Z. Evenson, B. Frick, F. Demmel, P. Fouquet and M. Karlsson, *Chem. Mater.*, 2023, **35**, 6713–6725.

36 A. Perrichon, M. Jiménez-Ruiz, L. Mazzei, S. M. H. Rahman and M. Karlsson, *J. Mater. Chem. A*, 2019, **7**, 17626–17636.

37 H. Yamamura, Y. Yamada, T. Mori and T. Atake, *Solid State Ion.*, 1998, **108**, 377–381.

38 Y. Uchimoto, M. Kinuhata, H. Takagi, T. Yao, T. Inagaki and H. Yoshida, *Proc. Vol.*, 1999, **1999–19**, 317.

39 T. Yao, Y. Uchimoto, M. Kinuhata, T. Inagaki and H. Yoshida, *Solid State Ion.*, 2000, **132**, 189–198.

40 C. Didier, J. Claridge and M. Rosseinsky, *J. Solid State Chem.*, 2014, **218**, 38–43.

41 H. Yamamura, H. Hamazaki, K. Kakinuma, T. Mori and H. Haneda, *J. Korean Phys. Soc.*, 1999, **35**, 200.

42 C. E. Mohn, N. L. Allan and S. Stølen, *Solid State Ion.*, 2006, **177**, 223–228.

43 V. Kahlenberg and C. Weidenthaler, *Solid State Sci.*, 2002, **4**, 963–968.

44 K. Saito, K. Fujii and M. Yashima, *J. Solid State Chem.*, 2022, **306**, 122733.

45 C. A. Fuller, J. I. Murrell, D. A. Blom, T. Vogt, W. Zhang, P. S. Halasyamani, I. R. Evans and J. S. O. Evans, *Chem. Mater.*, 2022, **34**, 3185–3196.

46 O. J. Wagstaff, M. Avdeev, S. J. Clark, J. S. O. Evans and I. R. Evans, *Chem. Mater.*, 2025, **37**, 3492–3503.

47 C. A. Fuller, D. A. Blom, T. Vogt, I. R. Evans and J. S. O. Evans, *J. Am. Chem. Soc.*, 2022, **144**, 615–624.

48 N. Kochetova, V. Cherepanova, A. Pikalova and A. Gilev, *Chim. Techno Acta*, 2024, **11**, 202411102.

49 A. A. Coelho, J. Evans, I. Evans, A. Kern and S. Parsons, *Powder Diffr.*, 2011, **26**, S22–S25.

50 R. E. Dinnebier, A. Leineweber and J. S. O. Evans, *Rietveld Refinement: Practical Powder Diffraction Pattern Analysis using TOPAS*, De Gruyter STEM, 2018, vol. 1.

51 H. M. Rietveld, *J. Appl. Crystallogr.*, 1969, **2**, 65–71.

52 A. M. Abakumov, R. V. Shpanchenko, O. I. Lebedev, G. Van Tendeloo, S. Amelinckx and E. V. Antipov, *Acta Crystallogr. A*, 1999, **55**, 828–839.

53 D. Waroquiers, X. Gonze, G.-M. Rignanese, C. Welker-Nieuwoudt, F. Rosowski, S. Göbel, S. Schenk, P. Degelmann, R. André, R. Glaum and G. Hautier, *Chem. Mater.*, 2017, **29**, 8346–8360.

54 R. D. Shannon, *Acta Crystallogr., Sect. A*, 1976, **32**, 751–767.

55 P. W. Stephens, *J. Appl. Crystallogr.*, 1999, **32**, 281–289.

56 R. Simura, Y. Suzuki and H. Yamane, *Acta Crystallogr., Sect. C: Struct, Chem.*, 2023, **79**, 464–471.

57 I. R. Evans, J. A. K. Howard and J. S. O. Evans, *Chem. Mater.*, 2005, **17**, 4074–4077.

58 V. Kahlenberg, R. X. Fischer and J. B. Parise, *J. Solid State Chem.*, 2000, **154**, 612–618.

59 R. A. Tamazyan, *Sov. Phys. - Crystallogr.*, 1987, **32**, 519.

60 J. Nielsen and M. Mogensen, *Solid State Ion.*, 2011, **189**, 74–81.

61 Y. L. Huang, C. Pellegrinelli and E. D. Wachsman, *J. Electrochem. Soc.*, 2015, **163**, F171.

62 J. Nielsen, A. Hagen and Y. L. Liu, *Solid State Ion.*, 2010, **181**, 517–524.

63 J. T. S. Irvine, D. C. Sinclair and A. R. West, *Adv. Mater.*, 1990, **2**, 132–138.

64 A. C. Lazanas and M. I. Prodromidis, *ACS Meas. Sci. Au*, 2023, **3**, 162–193.

65 M. Diaz-Lopez, J. F. Shin, M. Li, M. S. Dyer, M. J. Pitcher, J. B. Claridge, F. Blanc and M. J. Rosseinsky, *Chem. Mater.*, 2019, **31**, 5742–5758.

66 W. Zhang, K. Fujii, T. Ishiyama, H. Kandabashi and M. Yashima, *J. Mater. Chem. A*, 2020, **8**, 25085–25093.

67 Z. Cheng, Y. An, R. Wang, J. C. Neuefeind, X. Yang, R. Cong, T. Yang and P. Jiang, *Inorg. Chem.*, 2024, **63**, 22022–22032.

68 J. T. S. Irvine, J. W. L. Dobson, T. Politova, S. García Martín and A. Shenouda, *Faraday Discuss.*, 2007, **134**, 41–49.

69 A. Manthiram, J. F. Kuo and J. B. Goodenough, *Solid State Ionics*, 1993, **62**, 225–234.

70 D. Tyagi, A. N. Shirsat, B. Saha and S. Varma, *J. Alloys Compd.*, 2021, **877**, 160298.